# Study on the application effects of composite protective coatings on different metal surfaces



Na Li<sup>1</sup>

<sup>1</sup>Chemical Engineering Institute, Beijing University of Chemical Technology, Beijing, 100000, China

\*Corresponding Author: nkwalk223@gmail.com

Received: 12/08/2024 Revised: 10/06/2025 Accepted: 20/09/2025 Published: 26/10/2025

©2025 The Author(s). This is an open access article under the CC BY license https://creativecommons.org/licenses/by/4.0/

Abstract: Traditional corrosion prevention technologies such as electrochemical protection, corrosion inhibitors, and coatings can effectively mitigate metal corrosion issues. However, in recent years, this field has imposed increasingly stringent requirements beyond corrosion performance, demanding long-term protection, stability, and environmental adaptability for metals. To address these challenges, this study employs structural design to synthesize a series of novel carboxyl-functionalized polyarylenenitriles (CPENs) with varying molecular weights using bisphenol A, 2,6-dichlorobenzonitrile, and 2,6-dichlorobenzoic acid as raw materials. Performance testing and analysis of the CPEN coatings were conducted, including infrared analysis, stability, abrasion resistance, and acid/alkali corrosion resistance. Experimental tests on four metal substrates—steel, aluminum, copper, and magnesium—revealed that the presence of the coating shifted the corrosion potential toward the anodic direction compared to uncoated surfaces, while reducing the corrosion current density by one to two orders of magnitude. This demonstrates the coating's effective application on various metal surfaces.

**Keywords:** CPENs coating, stability, metal, corrosion protection

# 1 | Introduction

With the rapid advancement of modern industrial technology toward extreme conditions and intelligentization, reliability issues in mechanical systems under complex operating conditions—such as high temperatures, high pressures, high speeds, and multi-field coupling—have become increasingly prominent [1]. Composite coatings are widely applied in high-end equipment across aviation, aerospace, marine, and energy sectors, holding critical significance for both national economic development and defense capability enhancement [2, 3]. High-performance composite coatings serve as a protective shield for critical components of advanced equipment under demanding service conditions, ensuring their reliable operation [4]. Among these, organic-inorganic composite coatings combine the excellent film-forming properties of organic coatings with the superior weather resistance of inorganic coatings [5]. For instance, in the field of metal anti-corrosion coatings, alkali metal silicates and organosilicon compounds are frequently employed as key components [6]. Alkali metal silicates exhibit outstanding self-curing properties, film-forming capabilities, and water resistance [7]. Within organosilicon materials, silane coupling agents facilitate the bonding between organic and inorganic components in composite coatings [8].

In recent years, the preparation techniques, evaluation methods, and optimization strategies for composite protective coatings have proliferated, yielding significant research achievements [9, 10]. Li et al. [11] proposed a composite coating composed of fluorinated epoxy resin emulsion and in-situ modified dual-scale nanosilica. It exhibits a water contact angle of 158.6±1° and a sliding angle of 3.8±0.2°, maintaining stable properties under extreme acidic/alkaline conditions and temperatures, with outstanding weather resistance and superhydrophobicity. The graphene oxide/epoxy nanocomposite coating developed in [12] exhibited a corrosion rate of only  $6.10 \times 10^{-3}$  mil/year at a thickness of 10  $\mu$ m, with a charge transfer resistance of  $8.73 \times 10^{7}$   $\Omega \cdot cm^{2}$ after 90 days, demonstrating strong corrosion resistance and durability. Wang et al. [13] indicates that ZnO enhances graphene dispersion. It analyzed the influence of ZnO-graphene layer count on the anti-corrosion performance of ZnO-graphene/epoxy composite coatings, revealing that increased ZnO-graphene layers enhance both corrosion resistance and coating rigidity. Jiang et al. [14] designed a safe, environmentally friendly, and low-cost method for preparing composite water-based coatings. By copolymerizing polyvinylidene fluoride (PVDF) with seed emulsions of various acrylic monomers, the resulting composite coating exhibited excellent adhesion and weather resistance, maintaining its original gloss even under intense UV irradiation. Joshi et al. [15] evaluated the impact of nano-ceria and nano-zirconia on the weather resistance of polyurethane (PU)-based coatings. Changes in UV resistance coefficients and tensile properties were measured after 300 hours of exposure to specific UV irradiance, humidity, temperature, and wet/dry conditions. The weather resistance of PU/nano-ceria composites was superior to that of PU/nano-zirconia composites. Feng et al. [16] incorporated a composite material based on quaternized lignin sulfonate and tert-butyl titanate into a traditional water-based epoxy coating, yielding a high-performance QLS-TiO<sub>2</sub>/WEP composite coating. Leveraging the free radical scavenging capability and high chemical stability of the QLS-TiO2 layer, the composite coating demonstrated enhanced aging resistance and corrosion resistance. Majid et al. [17] developed a PU/GO-ZIF-7 coating using multiple materials. Under prolonged weathering, it exhibited minimal changes in aesthetic properties, chemical structure, and topological structure while demonstrating enhanced aging stability. This improvement stems from the hybrid mechanism of GO-ZIF-7 nanocomposites, which enhances the photostability of the PU coating. Oh et al. [18] leveraged the synergistic adsorption of hydrocarbons by rare earth oxides and hydrocarbon supply from hydrocarbon-based polymers to develop scalable CeO<sub>2</sub>/PDMS composite coatings. These coatings exhibit self-healing superhydrophobicity and excellent weather resistance, enabling them to withstand outdoor electrical insulation self-testing under 600V electrical stress.

The aforementioned composite coatings possess distinct characteristics that enhance the corrosion resistance, wear resistance, and impact resistance of metallic materials to varying degrees, thereby providing protective benefits. Additionally, Li et al. [19] presents an effective solution for the long-term preservation of wooden artifacts. Researchers incorporated perovskite nanosheets into a water-based acrylic resin, resulting in a composite coating with sufficient tensile strength, elastic modulus, toughness, and weather resistance to ensure the long-term storage of wooden artifacts. Azadi et al. [20] synthesized an organic-inorganic hybrid nanocomposite primarily composed of methyl methacrylate and 3-(trimethoxysilyl)propyl methacrylate. During preparation, tetraethyl orthosilicate and perfluorooctyl trichlorosilane were added to enhance the composite coating's heat resistance, weather resistance, and hydrophobicity. Results confirmed its suitability as a protective coating for stone cultural heritage. Guan et al. [21] achieved the organic integration of organophosphate-grafted  $\alpha$ -zirconium phosphate with melamine-formaldehyde resin. While maintaining transparency, this composite coating enhances fire resistance, smoke suppression, antibacterial properties, and weather resistance, thereby improving both the fireproofing and decorative performance of wood.

This paper first provides a detailed description of the experimental materials, instruments, and methods. By

introducing 2,6-dichlorobenzoic acid into the polymerization of bisphenol A-type polyarylene ether nitrile, a series of carboxyl-functionalized polyarylene ether nitriles (CPENs) with varying molecular weights were synthesized. Concurrently, a series of experiments were conducted to evaluate the performance of the protective coatings. Their structures were verified via infrared spectroscopy, while their thermal properties were investigated using DTG and TGA. Wear resistance and acid-alkali corrosion resistance were tested on various metal substrates, with long-term immersion experiments further validating the coatings' anti-corrosion properties. Finally, the stability of the coatings was analyzed and studied.

# 2 | Synthesis of CPENs

# 2.1 | Experimental Chemicals

The raw materials, their purities, and manufacturers used in the experiment are listed in Table 1.

TABLE 1 Experimental materials and reagents

Raw materials and reagents	Purity	Production enterprise
Bisphenol A	Hexafluorobisphenol A	Changzhou bofeng chemical co., LTD
Hexafluorobisphenol A	Hexafluorobisphenol A	fluorotechnology
2,6-dichlorobenzene	Hexafluorobisphenol A	Lianyungang Tianchen Chemical Co., LTD
2,6-chlorobenzoic acid	Hexafluorobisphenol A	Lianyungang Tianchen Chemical Co., LTD
Anhydrous potassium carbonate	Industrial pure	Jinan Huifeng Da Chemical Co., LTD
Toluene	Hexafluorobisphenol A	Tianjin Damao Chemical Reagent Factory
N-methylpyrrolidone	Hexafluorobisphenol A	Wuhan Haishan Technology Co., LTD
N, N-dimethylformamide	Hexafluorobisphenol A	Jinan Aotai Chemical Co., LTD
Dimethyl sulfoxide	Hexafluorobisphenol A	Jinan Yuanlian Chemical Co., LTD
Tetrahydrofuran	Hexafluorobisphenol A	Tianjin Jingqiang Chemical Co., LTD
Chloroform	Hexafluorobisphenol A	Jiaxing Ruiheng Biotechnology Co., LTD
Ethyl acetate	Hexafluorobisphenol A	Shanghai Yuanye Technology Co., LTD
Ethanol	Hexafluorobisphenol A	Tianjin Damao Chemical Reagent Factory
Petroleum ether	Hexafluorobisphenol A	Jiaxing Ruiheng Biotechnology Co., LTD
Hydrochloric acid	36%~38%	Tianjin Damao Chemical Reagent Factory

## 2.2 | Experimental Instruments

The names, models, and places of origin of the instruments and equipment used in the experiment are shown in Table 2.

TABLE 2 Laboratory instruments

Name	Model	Manufacturing enterprise
Fourier Transform infrared spectrometer	TENSOR 27	Bruker Spectrometers, Switzerland
Gel permeation chromatography	LC-20AD	Shimadzu Corporation of Japan
Differential scanning calorimetry analysis	Q20	TA Company, USA
Thermogravimetric analyzer	Q50	TA Company, USA
Dynamic thermomechanical analyzer	Q800	TA Company, USA
Electronic analytical balance	BSA2202S	Sartorius Group of Germany
Scanning electron microscope	IT 300	JEOL Co., Ltd. of Japan
Universal tensile testing machine	INSTRON-4467	Instron Laboratory Equipment Co., LTD
Cantilever beam impact testing machine	JJ-22	Jinan Chenxin Testing Machine Manufacturing Co., LTD
Magnetic stirring heating device	RCT basic	German IKA Company.
Vector network analyzer	Keysight E5071C	Agilent Technologies, Inc

## 2.3 | Synthesis of CPENs

## 2.3.1 | Synthesis mechanism

The synthesis of CPENs is based on a nucleophilic substitution reaction, occurring in three steps: dehydration, polymerization, and reduction.

#### (1) Dehydration Process

Both the hydroxyl group of bisphenol A and the carboxyl group of 2,6-dichlorobenzoic acid participate in this process. The diphenol reacts with  $K^+$  ions ionized from  $K_2CO_3$  to form a diphenol salt. Similarly, 2,6-dichlorobenzoic acid reacts with  $K^+$  to form a 2,6-dichlorobenzoate salt. The dehydration reaction between bisphenol A and 2,6-dichlorobenzoic acid is illustrated in Figure 1.

HO OH 
$$+K^{+} \rightarrow K0$$
 OK+H<sup>+</sup>

COOH COOH

CI CI +K<sup>+</sup> → CI CI +H<sup>+</sup>

CO<sup>2</sup><sub>3</sub> — H<sup>-</sup> → HCO<sub>3</sub> — H<sup>-</sup> → CO<sub>2</sub> + H<sub>2</sub>O

FIGURE 1 Dehydration reaction of bisphenol A with 2, 6-dichlorobenzoic acid

#### (2) Polymerization Process

This process involves the gradual polymerization of small-molecule monomers into macromolecular chains, including the nucleophilic substitution reaction between diphenylsulfone and 2,6-dichlorobenzonitrile and 2,6-dichlorobenzoic acid. 2,6-Dichlorobenzonitrile and 2,6-dichlorobenzoic acid share structural similarity, but the electron-withdrawing ability of the cyano group is stronger than that of the carboxyl group. Therefore, the chlorine atom attached to the benzene ring of 2,6-dichlorobenzonitrile reacts more readily with the dibasic

phenol salt than the chlorine atom on the benzene ring of 2,6-dichlorobenzoic acid. During the polymerization stage, monomers progressively polymerize onto the oligomer molecular chain, gradually growing into long CPEN chains. The polymerization process of carboxyl-containing polyarylenenitrile is illustrated in Figure 2.

FIGURE 2 The polymerization process of carboxyl-containing polyaryl ether sunny

#### (3) Reduction Process

This process involves the reduction of carboxylate groups on the side chains of polymer molecules and the reduction of phenolate groups at the molecular chain ends, completed during the post-reaction treatment stage. The reacted polymer is precipitated in hydrochloric acid solution. The crude product precipitated in the hydrochloric acid solution is collected, refluxed, washed with distilled water, and subjected to repeated refluxing and washing 3–5 times to thoroughly reduce the carboxylate and phenolate groups and remove residual ions. The reduction process for carboxyl-containing polyarylether nitrile is shown in Figure 3.

FIGURE 3 The reduction process of carboxyl-containing polyaryl ether sunny

#### 2.3.2 | Synthesis Process

The synthesis reaction was conducted in a four-neck flask equipped with a stirring paddle, water distributor, and thermometer, with nitrogen gas purging throughout. Bisphenol A, 2,6-dichlorobenzonitrile, 2, 6-dichlorobenzonic acid, and anhydrous K<sub>2</sub>CO<sub>3</sub>. After adding NMP and toluene in a 3:1 volume ratio, heating was initiated to start the reaction. The system was first heated to 150°C, where dehydration proceeded for 3 hours until no further water was formed. Toluene was then slowly removed by gradual heating, maintaining the reaction temperature at 200°C for 3 hours. The reaction was terminated when the system viscosity remained essentially constant.

After cooling, dilute with an appropriate amount of NMP to achieve a solid content <10%. Precipitate a white, fine powder in hydrochloric acid solution (0.1 mol/L). Reflux for 30 minutes to reduce phenol salts and carboxylate salts. Filter under vacuum and wash with distilled water. Repeat refluxing with hydrochloric

acid solution and washing with water at least three times to remove impurities. Finally, collect the product, dry it, and obtain a white carboxyl-containing polyarylethernitrile powder. A series of carboxyl-containing polyarylethernitriles with different molecular weights were synthesized according to the feed ratio. CPENs with different molecular weights are denoted as CPEN-n, where CPEN-20, CPEN-17, CPEN-13, CPEN-10 represent carboxyl-functionalized polyarylether nitriles with theoretical molecular weights of 20,000, 17,000, 13,000, and 10,000, respectively. The schematic diagram of CPEN synthesis is shown in Figure 4.

FIGURE 4 Schematic diagram of the synthesis of CPENs

# 2.4 | Preparation of CPENs/EP specimens

The carboxyl-functionalized polyarylethernitrile synthesized in this study exhibits a low glass transition temperature. Employing the hot-melt method to prepare CPENs/EP eutectic mixtures, a uniformly blended eutectic can be obtained by heating at 120°C for only 55 minutes, with the modified system maintaining relatively low viscosity at room temperature [22]. Compared to PEN, the synthesized CPENs exhibit reduced melting temperatures, shorter melting times, and simplified preparation processes.

In a beaker, EP and the corresponding CPENs were weighed according to mass ratios, heated to melt in a 120°C oven, and stirred vigorously every 10 minutes. After 50 minutes, a uniform CPENs/EP eutectic mixture was obtained. After cooling to 100°C, a calculated amount of 4,4'-diaminodiphenylmethane (MDA) was added and stirred until uniformly transparent, yielding the CPENs-modified EP resin system. Epoxy resin systems modified with polyarylene nitrile of different molecular weights are denoted as CPENs-X/EP.

An appropriate amount of CPENs/EP modified resin was applied to test specimens to prepare shear test specimens. The modified resin was poured into molds of various specifications to prepare tensile, flexural, impact, and DMA test specimens. The molds were placed in a 120°C oven for curing for 2.5 hours, then cooled to room temperature, yielding CPENs/EP modified epoxy resin specimens of multiple dimensions.

# 2.5 | Curing Mechanism of CPENs/EP

The CPENs/EP curing system comprises epoxy resin, the aromatic amine curing agent MDA, and the toughening agent CPENs. The curing process involves several reaction types. The primary reaction is between EP and MDA, as illustrated in Figure 5. The epoxy group first reacts with an active hydrogen atom of the

primary amine to form a secondary amine. The active hydrogen on the secondary amine then further reacts with the epoxy group to generate a tertiary amine, ultimately forming a network structure linked by nitrogen atoms [23].

$$\begin{array}{c} & & & & \\ & & & \\ & & & \\ & & & \\ & & & \\ & & & \\ & \\ & & \\ & & \\ & & \\ & & \\ & & \\ & & \\ & & \\ & & \\ & & \\ & & \\ & & \\ & & \\ & & \\ & & \\$$

#### FIGURE 5 Curing reaction of EP and MDA

Second is the reaction between EP and CPENs, as illustrated in Figure 6. The epoxy group can react with both the carboxyl side groups and terminal hydroxyl groups of CPENs. The flexible long chains of CPENs embed into the epoxy resin network structure, expanding the free volume of the epoxy resin and reducing its crosslink density.

#### FIGURE 6 Reaction between EP and CPENs

Reactions between CPENs and MDA may also occur within the CPENs/EP curing system, as illustrated in Figure 7. The active carboxyl groups may undergo sequential reactions with amino groups.

FIGURE 7 Reaction between CPENs and MDA

## 2.6 | Test Characterization

(1) Measure the contact angle (WCA) and spreading angle (SA) of the samples using a contact angle tester (Harke-SPCA). For contact angle testing, the droplet volume is  $6\mu$ L; for spreading angle testing, the droplet volume is  $10\mu$ L. Test each sample five times at different positions and take the average value.

- (2) Recorded the rolling and adhesion behavior of droplets on the sample surface using a video optical contact angle analyzer (OCA25). The droplet volume was  $10\mu$ L.
- (3) Conduct tape tests on the samples. Place the sample on a horizontal, smooth surface. Gently cover the sample surface with 2M transparent tape. Roll a weight back and forth over the tape three times, then peel off the tape. This constitutes one tape test cycle. Repeat this procedure for multiple tape tests.
- (4) The infrared spectrum of the sample surface was collected and analyzed using attenuated total reflection Fourier transform infrared spectroscopy (ATR-FTIR, Nicolet 6700), with a scanning range of 3000-500cm<sup>-1</sup>.
- (5) Tafel polarization curves (CHI660A) were recorded on an electrochemical workstation using a three-electrode system (test sample as working electrode, platinum sheet and saturated calomel electrode as counter and reference electrodes, respectively). Scanning was performed at 1 mV/s within the  $\pm 260$  mV vs. OCP voltage range. NaCl aqueous solution, pH=3 HCl solution, and pH=10 NH<sub>3</sub>·H<sub>2</sub>O solution.
- (6) Electrochemical impedance spectroscopy (EIS) was conducted in a 3.5 wt.% NaCl solution at open-circuit potential across a frequency range of  $10^5$  Hz to  $10^{-2}$  Hz, with an operating amplitude of 10 mV. The test area for all samples was approximately 1  $cm^2$ , with the remaining surface covered by insulating tape. Prior to testing, samples were immersed in the electrolyte solution until the system reached a stable open-circuit potential.

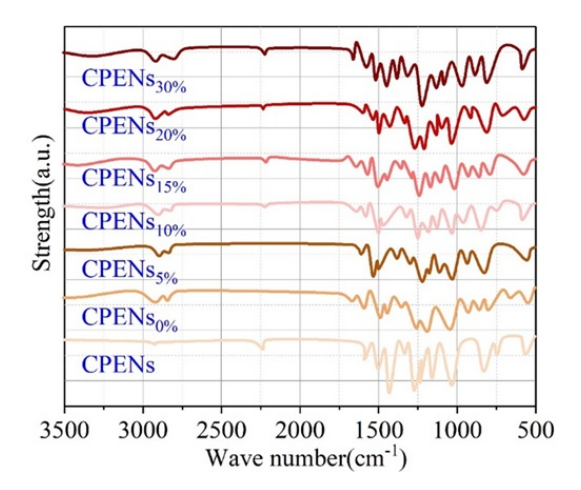


FIGURE 8 Infrared spectra of composite coatings with different ratios

# 3 | Experimental results and analysis

## 3.1 Infrared analysis results

#### 3.1.1 | Infrared spectrum of CPENs/EP composite coatings

FTIR characterization of CPENS/EP composite coating materials with varying ratios was conducted to verify the impact of PEN content changes on the chemical structure of EP. The infrared spectra of composite coatings with different ratios are shown in Figure 8. Except for variations in the intensity of the signal absorption peak at  $2225 \text{ cm}^{-1}$ , the remaining absorption peak signals in the infrared spectra of CPENs<sub>0%</sub>, CPENs<sub>5%</sub>, CPENs<sub>10%</sub>, CPENs<sub>15%</sub>, CPENs<sub>20%</sub>, and CPENs<sub>30%</sub> remained consistent, with no peak shifts or losses. This confirms that CPEN incorporation did not alter the chemical structure of EP. The characteristic infrared absorption peak at  $2225 \text{ cm}^{-1}$  originates from the symmetric stretching vibration of the cyano group on the benzene ring structure within CPENs. Consequently, as the mass fraction of added CPENs increases, the signal intensity of the characteristic cyano absorption peak at  $2225 \text{ cm}^{-1}$  progressively rises.

## 3.1.2 | Thermal Properties of CPEN/EP Composite Coatings

The TG and DTG curves of CPENs/EP composite coating materials at different ratios within the 50°C to 800°C range are shown in Figure 9 (Figure 9a displays the TGA curve of the composite coating, while Figure 9b shows the DTG curve). The impact of CPENs addition on the thermal stability of EP was evaluated by analyzing changes in sample weight loss and decomposition rate. As evident from the TG curve in Figure 9(a), the decomposition temperature at 4.7% weight loss (T5%) exceeded 370°C for all samples, demonstrating excellent high-temperature resistance. Compared to pure epoxy resin (CPENs<sub>0%</sub>), the T5% of composite samples showed no significant change with increasing PEN content. This indicates that CPENs introduction does not compromise the thermal stability of the epoxy resin, attributable to CPENs' inherently higher decomposition temperature than EP. The DTG curve (b) reveals two maximum thermal decomposition rate temperatures (Tmax) in the composite system. The first Tmax around 450°C corresponds to the decomposition peak of the less thermally stable EP component within the CPENs/EP composite. The second Tmax occurs around 512°C, representing the decomposition peak of the more thermally stable CPENs component in the composite system. Furthermore, the peak intensity of the EP component's Tmax diminishes with increasing CPENs content, indicating that CPENs can partially inhibit and slow down the thermal degradation of the epoxy resin.

The storage modulus and loss factor curves of composite coatings with different ratios are shown in Figure 10 (Figure 10a shows the storage modulus curve, and Figure 10b shows the loss factor curve). The storage modulus and loss factor  $(\tan\delta)$  of the CPENS/EP composite coating material were characterized using dynamic thermal mechanical analysis to investigate the trend of viscoelastic behavior changes in the CPENS/EP composite material. Figure 10(a) displays the storage modulus curves for CPENS/EP composites with varying ratios. It is evident that the storage modulus decreases from 1363 MPa (CPENs<sub>0%</sub>) to 1169 MPa (CPENs<sub>5%</sub>) when a small amount of CPENs is introduced. This phenomenon results from the reduced crosslinking density of the epoxy resin caused by the incorporation of CPENs. As the CPENs content further increases, the storage modulus of the composite exhibits a recovery trend, gradually rising from 1286 MPa at CPENs<sub>10%</sub> to 1685 MPa at CPENs<sub>30%</sub>. This can be explained by the fact that, with increasing content, CPENs gradually transforms from a dispersed phase to a continuous phase within the composite system, effectively restricting the migration

of epoxy molecular chains. Furthermore, when the CPENs content reached 15% by mass of the epoxy resin (CPENs<sub>15%</sub>), its storage modulus once again exceeded that of the pure epoxy resin.

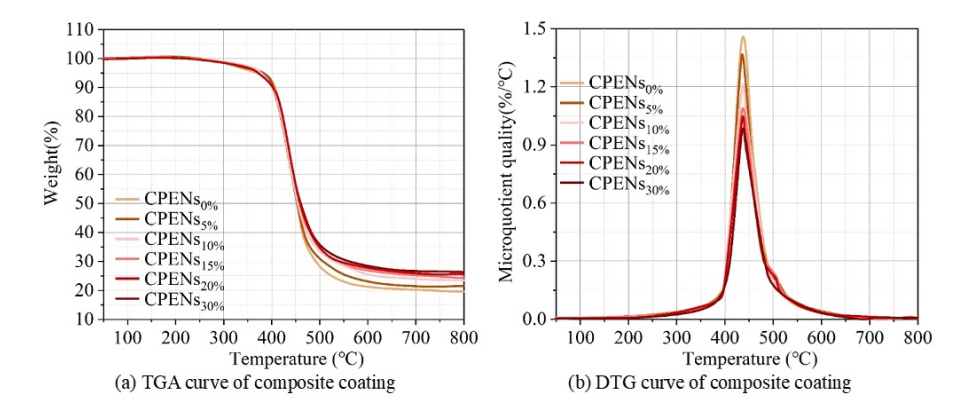


FIGURE 9 TGA and DTG curves of composite coatings of different ratios

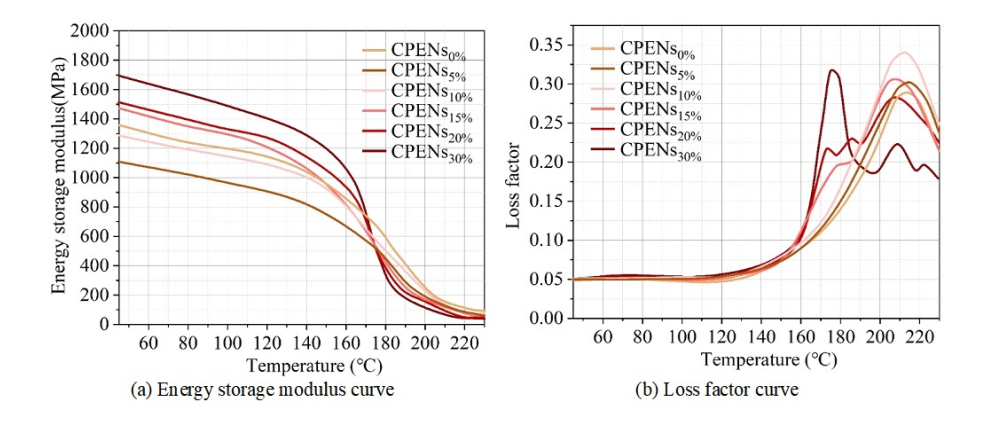


FIGURE 10 The storage modulus and loss factor curves of composite coatings

Figure 10(b) shows the loss factor curves of CPENs/EP composite coating materials at different ratios. Typically, the peak position of the loss peak can be defined as the glass transition temperature (Tg) of the epoxy polymer. The curves indicate that the pure EP coating (CPENs<sub>0%</sub>) exhibits only one loss peak at 214.5°C, which can be approximated as the Tg of pure epoxy. Upon CPENs addition, both CPENs<sub>5%</sub> and CPENs<sub>10%</sub> exhibit a shift in Tg toward lower temperatures, decreasing to 217.5°C and 215.2°C respectively. However, the curves still display only a single epoxy resin loss peak. This phenomenon can be explained as follows: at lower CPENs concentrations, CPENs exist as a dispersed phase within the epoxy matrix. At these levels, CPENs exhibit good dispersion within the EP coating without phase separation. However, as a dispersed phase, CPENs reduce the crosslinking density of the epoxy resin, thereby lowering the Tg of the CPENs/EP

composite coating material. As the CPENs content further increases, it forms a continuous phase structure within the EP matrix, restricting the molecular chain motion of the epoxy resin and thereby elevating the Tg of the composite material. Consequently, the Tg of the epoxy component in the CPENs<sub>15%</sub>, CPENs<sub>20%</sub>, and CPENs<sub>30%</sub> composite systems recovered to 207.8°C, 208.8°C, and 215.2°C, respectively. Additionally, at a CPENs content of 15% by mass of the epoxy resin (CPENs<sub>15%</sub>), a new, relatively weak loss peak appeared around 180°C, identifiable as the CPENs Tg. The appearance of dual loss peaks in the curve indicates phase separation in the CPENs/EP composite system. This demonstrates that at a CPENs content of 15% by mass of the epoxy resin, the increased CPENs content induces a phase transition within the EP matrix. The CPENs phase transforms from a dispersed phase to a continuous phase, resulting in a dual-continuous-phase structure within the CPENs/EP composite coating system.

## 3.2 | Corrosion resistance performance analysis results

Corrosion is the most troublesome issue encountered during the use of metallic materials, making it a critical factor that must be considered in the study of metal surfaces. Therefore, polarization curves and electrochemical impedance spectra of steel, aluminum, copper, and magnesium with and without coatings were obtained through electrochemical corrosion testing in a 3.5% NaCl solution. This enabled the evaluation of the corrosion resistance of CPENs/EP composite coatings on different metal substrates.

#### 3.2.1 | Polarization curve

Using the SP-150 electrochemical workstation, polarization curves were obtained for four metal substrates with and without coatings through electrochemical corrosion testing in a 3.8% NaCl solution. The polarization curves for different metal substrates with and without coatings are shown in Figure 11 (a–d represent steel, aluminum, copper, and magnesium, respectively).

Using the Tafel extrapolation method, the corrosion potential (Ecorr) and corrosion current density (Icorr) of the four metal substrates with and without coatings were obtained. The corrosion potential and corrosion current density of the four metal substrates with and without coatings are shown in Table 3. Higher corrosion potential and lower corrosion current density indicate better corrosion resistance.

TABLE 3	The corrosion	potential and	l corrosion	current der	nsity

Metal matrix type	With or without coating	$E_{corr}(V)$	$I_{corr}(A/cm^2)$
Steel	No	-0.684	$2.9 \times 1^{0-6}$
	Yes	-0.256	$1.03 \times 10^{-7}$
Aluminium	No	-0.826	$3.68 \times 10^{-6}$
	Yes	-0.45	$8.27 \times 10^{-8}$
Copper	No	-0.29	$4.05 \times 10^{-7}$
	Yes	-0.222	$1.98 \times 10^{-8}$
Magnesium	No	-0.188	$9.15 \times 10^{-5}$
	Yes	-0.134	$8.29 \times 10^{-7}$

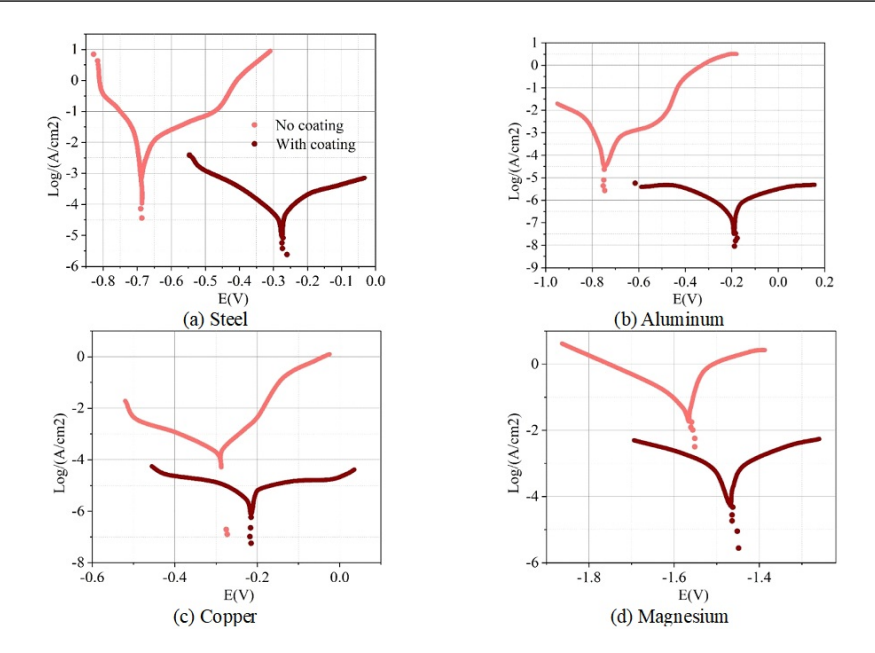


FIGURE 11 Polarization curves of different metal substrates with and without coatings

As shown in the chart, the corrosion potential of the four metal substrates—steel, aluminum, copper, and magnesium—shifts toward the anodic direction when coated compared to uncoated surfaces, with the corrosion current density decreasing by one to two orders of magnitude. This indicates that coating the surface significantly enhances the corrosion resistance of the metal substrate compared to its bare state.

#### 3.2.2 | Electrochemical impedance spectroscopy

Electrochemical impedance is also a crucial indicator for evaluating corrosion resistance. Higher electrochemical impedance indicates superior corrosion resistance of the test sample. Figure 12 shows the electrochemical impedance spectra of coated and uncoated samples of steel, aluminum, copper, and magnesium in a 3.6% NaCl solution (a–d represent steel, aluminum, copper, and magnesium, respectively). Figure 12(a) shows the EIS curve for steel. The maximum impedance of the uncoated sample is approximately 3100  $\Omega \cdot cm^2$ , while that of the coated sample reaches about 8900  $\Omega \cdot cm^2$ . Figure 12(b) shows the EIS curve for aluminum. The maximum impedance of the uncoated sample is approximately 5100  $\Omega \cdot cm^2$ , while that of the coated sample is approximately 21000  $\Omega \cdot cm^2$ . Figure 12(c) shows the EIS curve for copper. The maximum impedance of the uncoated sample was approximately 1100  $\Omega \cdot cm^2$ , while that of the coated sample was approximately 8100  $\Omega \cdot cm^2$ . Figure 12(d) shows the EIS curve for magnesium. The maximum impedance of the uncoated sample was approximately 350  $\Omega \cdot cm^2$ , while that of the coated sample was approximately 8000  $\Omega \cdot cm^2$ . The electrochemical impedance curves of coated and uncoated surfaces for these four metals demonstrate that the presence of CPENs/EP composite coatings on the metal substrate significantly enhances the samples' impedance values. This indicates that the CPENs/EP composite coating markedly improves the corrosion

resistance of the metal substrate, providing excellent protective properties for the metal.

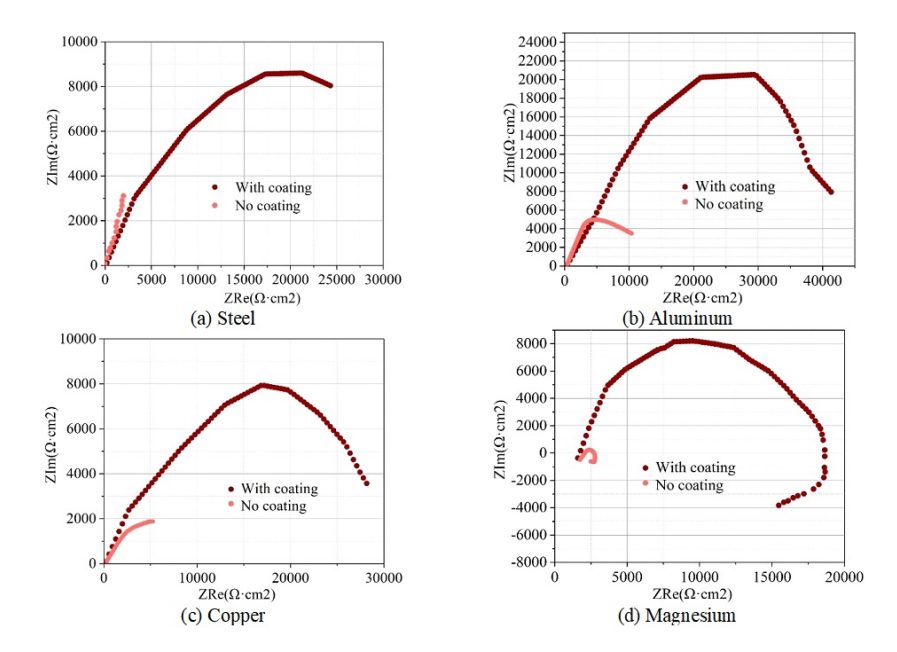
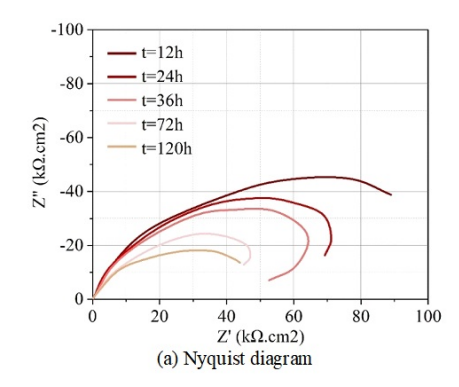


FIGURE 12 EIS curves of different metal substrates with and without coatings

#### 3.2.3 | Immersion degradation behavior

To thoroughly evaluate the long-term anti-corrosion performance of CPENs/EP composite coatings in corrosive media, this study employed a combined approach of electrochemical impedance spectroscopy (EIS) and microstructural characterization. It demonstrated the immersion degradation behavior of the CPENs/EP composite coating in a 3.5 wt% NaCl solution. By comparing the electrochemical impedance spectra and SEM images of bare copper substrates and CPENs/EP composite coatings after different immersion durations at room temperature, the coating's long-term anti-corrosion performance was confirmed. NaCl solution. Electrochemical impedance spectra (EIS) and scanning electron microscopy (SEM) images of bare copper substrates and CPENs/EP composite coatings after different immersion durations at room temperature were compared to demonstrate the coating's long-term corrosion resistance and surface morphology changes. The evolution of Nyquist plots and Bode plots for the coating immersed in 3.5 wt% NaCl aqueous solution for 120 hours is shown in Figure 13 (Figure 13a: Nyquist plot; Figure 13b: Bode plot). The Nyquist plot of the pure copper sample at the initial immersion stage (0 hours) exhibits a single capacitive arc, corresponding to charge transfer resistance (Rct) and double-layer capacitance (CPEdI), indicating the poor effectiveness of the natural oxide film on the pure copper surface. As immersion time extended to 120 hours, the radius of the capacitive arc significantly decreased, with pronounced inductive characteristics emerging in the low-frequency region. Phase angle variations indicate that the corrosion process is regulated by multiple surface state variables, such as Cl<sup>-</sup> adsorption-induced localized acidification and the dynamic deposition/dissolution of corrosion products.

In contrast, the CPENs/EP composite coating sample exhibited a dual capacitive arc pattern at the initial stage (0 hours). The high-frequency capacitive arc corresponded to the coating body impedance (Rf), while the mid-frequency region reflected the coating/substrate interface characteristics (Rct). The low-frequency impedance modulus reached 45 k $\Omega \cdot cm^2$ , confirming the coating's excellent anti-corrosion performance. As immersion time increased, both the high-frequency capacitive arc diameter and impedance modulus gradually decreased. Nevertheless, after 120 hours of immersion, the low-frequency impedance modulus of the CPENs/EP composite coating retained 20 k $\Omega \cdot cm^2$ , demonstrating that although partial physical degradation occurred, the remaining coating still provided satisfactory corrosion protection.



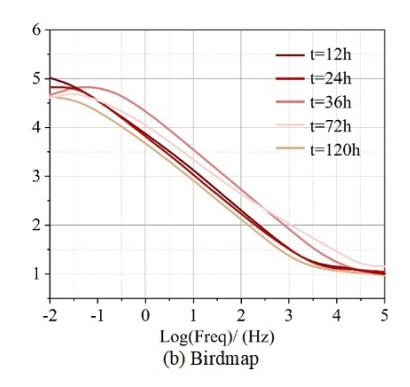


FIGURE 13 The evolution of the nequesett and the berdgram

## 3.3 | Coating stability test

The mechanical and chemical stability of the anti-corrosion test coating was evaluated through tape stripping, water impact, sandpaper abrasion, and acid-base-salt immersion tests. The evolution of the water contact angle on the CPENs/EP composite coating surface under different factors is shown in Figure 14 (Figure 14a: number of tape stripping cycles; Figure 14b: immersion time; Figure 14c: wear distance; Figure 14d: sandpaper abrasion distance). The optimized coating's mechanical stability was evaluated via tape stripping. As shown in (a), the initial water contact angle (WCA=104.2°) of the CPENs/EP composite coating deviated by less than 1° from the recorded value, validating the process reproducibility of hydrophobic group distribution. After 250 peel cycles, the cumulative WCA change was strictly controlled within  $6^{\circ}$  (104.2°  $\rightarrow$  99.9°), consistent with the 5° decay observed in the original data. No abrupt structural failure of the multilayer was observed during peeling. As shown in Figure 14(b), chemical tolerance testing of the optimized coating using solutions of varying acid/base concentrations and sodium chloride demonstrated that the functionally enhanced coating maintained its original protective efficacy under extreme conditions. In an acidic environment (pH=5), the WCA decreased from 100.5° to 98.5° before stabilizing, exhibiting less than 1% deviation from the data, with no change in proton permeation rate due to process adjustments. In an alkaline environment (pH=9), characteristic fluctuations of  $99.7^{\circ} \rightarrow 100.9^{\circ} \rightarrow 99.8^{\circ}$  were observed, with maximum deviations at each point not exceeding 2° from the original records, confirming that the molecular structure remained unaffected by the optimization. The standard deviation of the final stable WCA values in all three experimental sets was less than

2°, indicating that the process optimization introduced no risk of chemical stability degradation. As shown in Figure 14(c), dynamic hydraulic load testing of the optimized coating demonstrated structural integrity comparable to the original system. The decay curve showed WCA decreasing from 107.4° to 95.3° post-impact, while the critical failure water volume remained at 1500 mL. This confirms that the optimization process did not alter the coating's dynamic wetting properties, providing equivalent reliability assurance for applications in outdoor equipment subjected to rain erosion scenarios. As shown in Figure 14(d), mechanical abrasion testing was conducted on the CPENs/EP composite coating. After a 60cm abrasion cycle, the WCA remained above 94°. WCA fluctuations within the 40–60 cm range were strictly controlled within 0.6°, outperforming the 1° fluctuation limit of the original data.

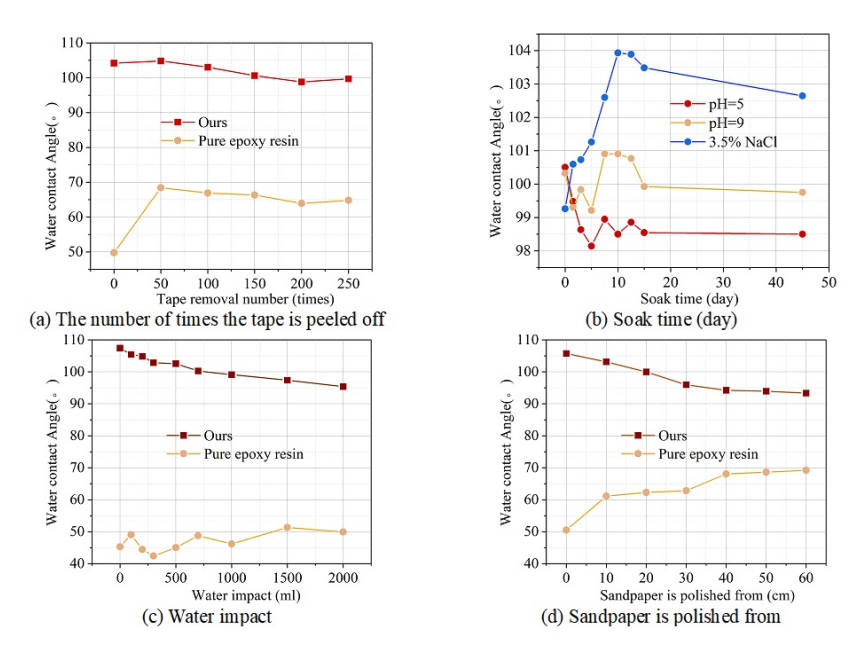


FIGURE 14 Evolution of water contact angle

# 4 | Conclusion

In this study, four molecular weight grades of carboxyl-functionalized polyarylenenitrile (CPENs) were synthesized. A series of experiments validated the superior performance of the proposed composite protective coating. The research conclusions are as follows:

Polarization curve testing revealed that even after 120 hours of immersion, the low-frequency impedance modulus of the CPENs/EP composite coating retained 20 k $\Omega \cdot cm^2$ , demonstrating excellent corrosion protection.

Mechanical abrasion testing showed that the optimized coating maintained a WCA above  $94^{\circ}$  after a 60 cm abrasion cycle, with WCA fluctuations strictly controlled within  $0.6^{\circ}$  between 40-60 cm—significantly

outperforming the 1° fluctuation limit of the original data and demonstrating excellent stability.

The study validated the universality of the designed composite protective coating across various metal surfaces, suggesting promising application prospects for preparing coatings on a broader range of metallic substrates.

#### References

- [1] Worden, K., Staszewski, W. J., & Hensman, J. J. (2011). Natural computing for mechanical systems research: A tutorial overview. *Mechanical Systems and Signal Processing*, 25(1), 4-111.
- [2] Karmakar, R., Maji, P., & Ghosh, S. K. (2021). A review on the nickel based metal matrix composite coating. Metals and Materials International, 27(7), 2134-2145.
- [3] Ren, Y., Zhang, L., Xie, G., Li, Z., Chen, H., Gong, H., ... & Luo, J. (2021). A review on tribology of polymer composite coatings. Friction, 9(3), 429-470.
- [4] Fayomi, O. S. I., Akande, I. G., Abioye, O. P., & Fakehinde, O. B. (2019). New trend in thin film composite coating deposition: a mini review. *Procedia Manufacturing*, 35, 1007-1012.
- [5] Liu, F., Liu, A., Tao, W., & Yang, Y. (2020). Preparation of UV curable organic/inorganic hybrid coatings-a review. Progress in Organic Coatings, 145, 105685.
- [6] Parashar, G., Srivastava, D., & Kumar, P. (2001). Ethyl silicate binders for high performance coatings. Progress in Organic Coatings, 42(1-2), 1-14.
- [7] Tomar, A. S., Gupta, R., Bijanu, A., Arya, R., Mishra, D., Singh, A., & Salammal, S. T. (2022). Progress in fabrication and manufacturing of sodium aluminosilicate materials (geopolymers) as protective coating materials: A review. *Journal of Polymer Research*, 29(6), 239.
- [8] Mai, C., & Militz, H. (2004). Modification of wood with silicon compounds. Treatment systems based on organic silicon compounds—a review. Wood Science and Technology, 37(6), 453-461.
- [9] Jena, G., & Philip, J. (2022). A review on recent advances in graphene oxide-based composite coatings for anticorrosion applications. Progress in Organic Coatings, 173, 107208.
- [10] Yar-Mukhamedova, G. S., Zellele, D. M., Rutkowska-Gorczyca, M., Makhambet, I., Mussabek, G., Atchibayev, R., & Kemelzhanova, A. (2025). Advancements in Coating Methods and Properties of Titanium-Based Composite Coatings: A Review. ES Materials & Manufacturing, 28, 1569.
- [11] Li, J. H., Weng, R., Di, X. Q., & Yao, Z. W. (2014). Gradient and weather resistant hybrid super-hydrophobic coating based on fluorinated epoxy resin. *Journal of Applied Polymer Science*, 131(20).
- [12] Li, Z. J., Wang, F. S., Lai, Y. C., Shi, Z. E., & Yu, Y. H. (2021). Flexible epoxy graphene thermoset with excellent weather and corrosion resistance. Progress in Organic Coatings, 151, 106052.
- [13] Wang, Y., Ma, L., Niu, Y., Ma, H., Lv, Y., & Lv, K. (2025). Shell-like ZnO-Graphene/Epoxy Coating with Outstanding Anticorrosion Performance and Weather Resistance. Coatings, 15(1), 63.
- [14] Jiang, Y., Pan, M., Yuan, J., Wang, J., Song, S., & Liu, G. (2020). Fabrication and structural characterization of poly (vinylidene fluoride)/polyacrylate composite waterborne coatings with excellent weather resistance and room-temperature curing. Colloids and Surfaces A: Physicochemical and Engineering Aspects, 598, 124851.
- [15] Joshi, M., Sandhoo, R., & Adak, B. (2022). Nano-ceria and nano-zirconia reinforced polyurethane nanocomposite-based coated textiles with enhanced weather resistance. Progress in Organic Coatings, 165, 106744.

[16] Feng, P. X., Xie, Y. H., Chen, X. Y., Li, J. F., Luo, Y. R., Feng, Y. H., & Wang, H. (2025). Constructing lignin functional coatings for intelligent protection through interface engineering technology: exhibiting excellent anti-corrosion and weather resistance: P.-X. Feng et al. Rare Metals, 1-12.

- [17] Majidi, R., Keramatinia, M., Ramezanzadeh, B., & Ramezanzadeh, M. (2023). Weathering resistance (UV-shielding) improvement of a polyurethane automotive clear-coating applying metal-organic framework (MOF) modified GO nano-flakes (GO-ZIF-7). Polymer Degradation and Stability, 207, 110211.
- [18] Oh, S., Shim, J., Seo, D., Shim, M. J., Han, S. C., Lee, C., & Nam, Y. (2022). Organic/inorganic hybrid cerium oxide-based superhydrophobic surface with enhanced weather resistance and self-recovery. *Progress in Organic Coatings*, 170, 106998.
- [19] Li, Z., Ye, Y. N., Kang, B., Hua, Y., Wang, Z., Yan, D., ... & Zhu, S. (2025). High-transparency, weather-resistant nanocomposite coatings from a shear-aligned 2D unit-cell-thick perovskite for wooden artifact preservation. *Journal of Materials Chemistry A*, 13(16), 11547-11556.
- [20] Azadi, N., Parsimehr, H., & Ershad-Langroudi, A. (2020). Cultural heritage protection via hybrid nanocomposite coating. Plastics, Rubber and Composites, 49(9), 414-424.
- [21] Guan, J., Wei, Z., Yan, L., Tang, X., & Xu, Z. (2024). Construction of organophosphate-functionalized α zirconium phosphate towards fire-resistant, weather-resistant and antibacterial reinforcement of transparent fire-proof coatings applied on wood substrates. Progress in Organic Coatings, 190, 108397.
- [22] Tiss, B., Martínez-Martínez, D., Mansilla, C., Gomes, J. M. R., Abreu, C. S., Pereira, N., & Cunha, L. Protective Coatings for Complex Organic Flexible Materials Ii: Improvement of Tribological Performance of Three Different Rubbers by Deposition of Tio<sub>2</sub> and Zno Films by Magnetron Sputtering. Available at SSRN 5231237.
- [23] Nakai, Y., Teruuchi, Y., Takeuchi, M., Nagatani, A., Oishi, A., Hagihara, H., & Watanabe, R. (2025). Room-temperature processed epoxy-silica nanocomposite coating for improved hardness and UV protection of polycar-bonate. Polymer Degradation and Stability, 238, 111329.